Early structural build-up behavior, setting mechanism, and nanostructure of alkali-activated GGBFS mixtures

Dai, Xiaodi; Aydin, Serdar; Yardimci, Mert Yuecel; REEKMANS, Gunter; ADRIAENSENS, Peter & De Schutter, Geert (2023) Early structural build-up behavior, setting mechanism, and nanostructure of alkali-activated GGBFS mixtures. In: JOURNAL OF THE AMERICAN CERAMIC SOCIETY, 107 (1) , p. 567 -592.

DOI: 10.1111/jace.19458
Handle: http://hdl.handle.net/1942/41673

Early structural build-up behavior, setting mechanism and nanostructure of alkali-activated GGBFS mixtures

Xiaodi DAI[1,2*], Serdar AYDIN[3], Mert Yücel YARDIMCI[1,4], Gunter REEKMANS[5], Peter ADRIAENSENS[5], Geert DE SCHUTTER[1].

1. Magnel-Vandepitte Laboratory, Department of Structural Engineering and Building Materials, Ghent University, Zwijnaarde 9052, Ghent, Belgium
2. Laboratory for the Chemistry of Construction Materials (LC[2]), Department of Civil and Environmental Engineering, University of California, Los Angeles, CA, 90095, USA
3. Department of Civil Engineering, Dokuz Eylül University, Buca 35160, Izmir, Turkey
4. Department of Civil Engineering, Istanbul Okan University, Tuzla, 34959, Istanbul, Turkey
5. Analytical and Circular Chemistry (ACC), Institute for Materials Research (IMO), Hasselt University, Agoralaan 1, 3590 Diepenbeek, Belgium.
*corresponding author: Xiaodi.Dai@Ugent.be

Abstract

The initial changes in the microstructure of Alkali-activated slag cement (AAS) characterize the rheological behavior, initial structuration and setting times of the mixture. In this study, the relationships between the rheological behavior, solidification process and nanostructure changes of sodium hydroxide-activated slag (NH-AAS) and sodium silicate-activated slag (SS-AAS) pastes over time are investigated by small amplitude oscillation test, isothermal calorimetry, SEM analyses and ^{1}H-^{29}Si cross-polarization magic angle spinning nuclear magnetic resonance spectroscopy (CP MAS NMR) and ^{29}Si MAS NMR spectroscopy. Test results showed that the NH-AAS reaches its initial setting time following a continuously proceeding structuration process, while the SS-AAS reaches its initial setting with an abrupt increase in the structuration process. At their initial setting times, the NH-AAS and SS-AAS mixtures release similar heat and reach a similar reaction degree. The SS-AAS mixture had more N-A-S-H formation than C-A-S-H at the initial setting time. On the other hand, the amount of C-A-S-H was similar to N-A-S-H in the NH-AAS mixture. The gradual N-A-S-H gel degradation to form C-A-S-H was observed during the acceleration period for the SS-AAS mixture.

Keywords: *Structural build-up, Setting time, Nanostructure, Nuclear magnetic resonance spectroscopy (NMR), Alkali-activated cements, Ground granulated blast furnace slag.*

1. Introduction

Alkali-activated cement (AAC) has been considered as a low carbon footprint alternative to Portland cement (PC) due to its higher mechanical properties, better volume stability, and greater resistance to sulfate and acid attack depending on the precursor type [1]. Alkali-activated slag cement (AAS) is a common and promising type of AAC, as their production uses ground granulated blast furnace slag (GGBFS), an industrial by-product, and substantially reduces the CO_2 emission [2], [3]. However, although numerous studies have explored the mechanical properties and durability of AAS [2]–[5], very few studies have focused on their microstructural changes over time influencing the rheological properties and setting behavior [6], [7].

The rise in structural build-up of cementitious materials results from the combination of physical interactions and chemical hydration [7], [8]. In Portland cement, the setting process can roughly be divided into three stages: (i) a colloidal percolation network is formed due to colloidal interactions between cement particles, (ii) cement particles are rigidly connected by the early reaction products such as nano-size C-S-H bridges, (iii) C-S-H bridges are further strengthened, leading to a percolated rigid network [9]. Recently, a few authors have also explained the increase in the early structural build-up of AAC. Alnahhal et al. [10] compared the viscoelastic behavior between alkali-activated slag/fly ash and cement pastes and found that the colloidal attraction between cement particles was significantly stronger than the cohesiveness of the very early inter-particle gel contacts generated in alkali-activated slag/fly ash pastes. They stated that the accumulation of initial reaction products was a possible reason for reaching the solid-like state in the sodium silicate-activated mixtures. In contrast, reaching the solid-like state resulted from a well-percolated network formation in cement paste. Furthermore, another study [8] also pointed out that sodium hydroxide-activated mixtures could also present a percolation network in the early times, a similar setting process with cement pastes. Kashani et al. [11] also investigated the relationship between surface chemistry and rheology in AAS pastes. The authors found that the yield stress was dependent on the changes in the surface chemistry by the amount of activation solutions. For example, a small addition of sodium silicate increased the zeta

potential, showing the increase in double-layer repulsive forces reducing the yield stress of AAS pastes. On the other hand, a further increase in sodium silicate amount increased the yield stress, possibly due to the increase in pH causing more slag dissolution resulting in the formation of reaction products.

The understanding of the change in the nanostructure of AAS from mixing to initial setting time is also crucial. Palacios et al. [12] reported that the rapid loss of fluidity and fast setting of sodium silicate-activated mixtures is due to the initial precipitation of ill-defined N-A-S-H and C-N-A-S-H products. Li et al. [13] used various combined activators to understand the setting and hardening control of AAS. They elucidated that Ca (and hence also Mg) acts as a network modifier in slag glass, causing these precursors to dissolve more quickly. Fly ash, on the other hand, does not exhibit the same level of reactivity due to its chemical stability.

Acquiring knowledge of the nanostructure of AAS will also enable the industry to develop new strategies to design AAS mixtures and promote their applications. The nanostructure characterization of AAS can be done in different ways. For example, Chen et al. [14] used Fourier-transform infrared spectroscopy (FTIR) and observed that the Q^2 band shifted to larger wavenumbers and became broader with an increase of silicate modulus in the activator solution. Puertas et al. [15] used various techniques, such as X-ray diffraction (XRD), FTIR and nuclear magnetic resonance (NMR), to determine the structure and composition of the main reaction products. Ismail et al. [16] used environmental scanning electron microscopy (ESEM) with energy dispersive X-ray (EDX) to determine the gel composition. They reported that the silicate-activated slag showed a nanostructure dominated by a C-A-S-H type gel. In contrast, silicate-activated fly ash was dominated by N-A-S-H 'geopolymer' gel formations. However, all of the abovementioned studies have focused on the later ages of AAC and cannot provide enough information about the microstructural changes at very early ages.

Therefore, this study aims to determine the early gel composition of AAS at the initial setting time and investigates the relationship between the early structural build-up and nanostructure of AAS. The

structural build-up of AAS has been evaluated by small amplitude oscillation sweep (SAOS) tests. The nanostructure of AAS was determined by the combined use of ^{1}H-^{29}Si cross-polarization magic-angle spinning NMR (CPMAS NMR) and ^{29}Si MAS NMR. The rheological behavior and gel composition of sodium hydroxide-activated (NH-AAS) and sodium silicate-activated slag mixtures (SS-AAS) at the initial setting time was compared.

2. Materials and Methods

2.1 Materials and mix design

In this investigation, ground granulated blast furnace slag (GGBFS) was employed as precursor. This material was provided by ORCEM, the Netherlands. Table 1 displays the results of the chemical composition analyzed by X-ray fluorescence (XRF). The X-ray diffraction pattern and particle size distribution of GGBFS are displayed in Fig. 1. A broad diffraction hump between 20º and 35º 2θ is observed due to the presence of the amorphous components and the absence of crystalline phases. GGBFS has a volume-mean particle sizes (d_{50}) of around 9 μm. Sodium hydroxide pellets (NaOH, caustic soda) with 97 % purity and liquid sodium silicate solution were used as activating agents. The liquid sodium silicate solution consists of 28.5% SiO_2, 17.95% Na_2O and 53.55% water with an Ms value (SiO_2/Na_2O) of 1.6. Sodium hydroxide was used to adjust the Ms value of the activator solution to 1.2. The mixture compositions are given in Table 2. Two AAS mixtures were produced in this study; the mixtures coded as NH-AAS was activated by NaOH, while the mixtures coded as SS-AAS was activated by the combination of NaOH and liquid sodium silicate with a Ms value of 1.2. The water-to-solid binder ratio (w/sb) and sodium content (Na_2O%) of the mixtures NH-AAS and SS-AAS were 0.45 and 5%, respectively. The pH values of activator solutions (Table 2) were determined by a pH meter at 20 ºC. However, it should be noted that using a pH meter to measure the pH of the activator solutions may result in some errors owing to the extremely high alkali ion concentrations and the presence of silica in the activator solution [17].

Table 1. Chemical composition of the GGBFS.

Precursor	CaO	SiO_2	Al_2O_3	MgO	SO_3	TiO_2	K_2O	Na_2O	Fe_2O_3	MnO	Others
GGBFS	40.8	33.3	12.3	7.84	2.30	1.29	0.67	0.44	0.39	0.36	0.31

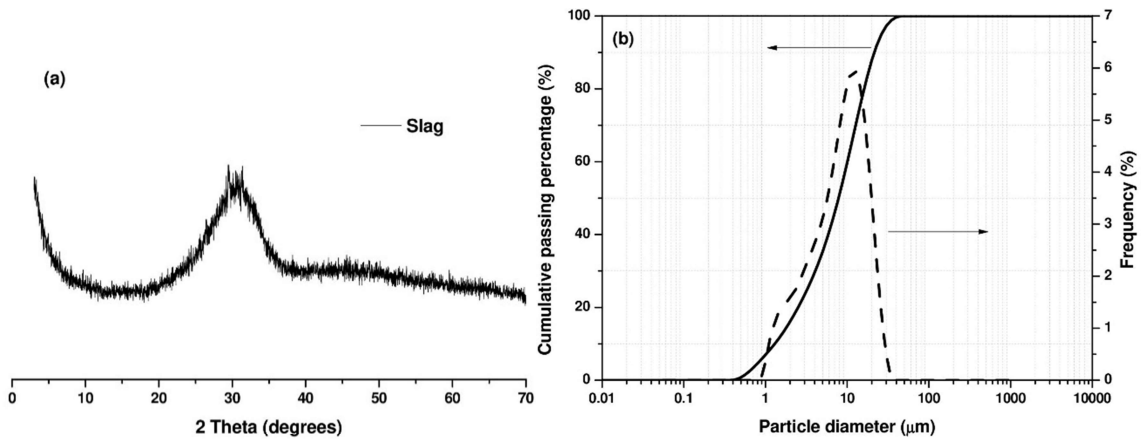

Fig. 1. X-ray diffraction pattern (a) and Particle size distribution (b) of GGBFS.

Table 2. Mixture design of AAS.

Mixture notation	Activator nature	W/SB ratio	Ms ratio	Na_2O (%)	SiO_2 (%)	pH	Initial setting time (min)
NH-AAS	Sodium hydroxide	0.45	0	5	0	13.82	120
SS-AAS	Sodium hydroxide and sodium silicate	0.45	1.2	5	6	13.50	45

2.2 Sample preparation

The activator solutions were prepared one day before usage to ensure the complete dissolution of NaOH. To prepare the paste samples for rheological tests and microstructural analysis, the GGBFS

and the activator solution were mixed in a plastic container using a mechanical stirrer for 30 s at 200 rpm followed by 3 min at 1800 rpm.

2.3 Experimental methods

2.3.1 Structural build-up and setting times of AAS pastes

Small amplitude oscillation shear (SAOS) tests were carried out in an oscillatory rheometer (Anton Paar MCR 102) to assess the structural build-up of AAS pastes. Storage modulus measurements were used as an indicator of the elastic portion of the mixtures. All the tests in this study were carried out at a temperature of 20 ºC.

The testing geometry was a six-blade vane in a steel cylindrical cup, which was used to eliminate the effect of slippage between the paste and the plate or the cylindrical cup during measurements [7], [18]. A plastic cover was placed on the top of the cup to prevent evaporation. Prior to time-sweep tests, the linear viscoelastic region (LVER) was determined by the strain-sweep test, which was a test that the strain amplitude was increased from 0.0001% to 20% with a constant frequency of 1 Hz. The strain-sweep test results are presented in Fig. 2. The strain amplitude of 0.005% was chosen in time-sweep tests to ensure two mixtures were tested in LVER [6], [7], [19], [20]. The AAS paste was then subjected to pre-shear at 100 s^{-1} for 30 s and rest for another 30 s to eliminate the residual stress. The SAOS time-sweep tests were immediately started at the age of 6 min.

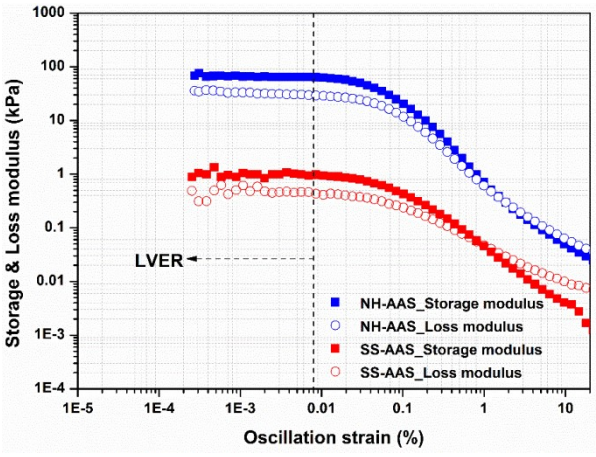

Fig. 2. Strain-sweep of AAS pastes for the determination of the LVER.

An automatic Vicat apparatus was used to determine the setting times of AAS pastes. The initial setting times of AAS pastes were determined when the needle penetration depth reached 6 ± 3 mm according to EN196-3 standard [21].

2.3.4 Heat evolution of AAS pastes

The calorimetric curves of AAS pastes were measured by eight-channel isothermal calorimetry (TA instrument, USA). After mixing, the AAS pastes were immediately placed into a glass ampoule; afterward, the ampoule was sealed and loaded into the isothermal calorimetry. The calorimetric measurements were carried out at a temperature of 20 °C for 3 days.

2.3.5 ^{1}H-^{29}Si solid-state cross-polarization magic angle spinning nuclear magnetic resonance (CPMAS NMR) and ^{29}Si MAS NMR analysis

It is important to select an appropriate technique to stop the reactions prior to ^{1}H-^{29}Si CPMAS NMR and ^{29}Si MAS NMR tests. In this study, the method to arrest the hydration of AAS was followed by Chen et al. [23]. Firstly, the fresh pastes were mixed with deionized water and then subjected to centrifugation to remove the liquid. This water extraction was repeated two times to remove the soluble silicate species. Afterwards, a chemical extraction was carried out in a way that the solid part was put on the 0.2 μm nylon filter membrane, and then at least 400 ml solvent (50/50 volume of methanol/acetone) was added to wash the solid part and remove the water. Before NMR analysis, the residual particles were collected and stored in a mild vacuum condition for 24 hours. Palacios et al. [12] also noted that the initial washing of the AAS pastes with water and subsequent treatment with isopropanol also can be an appropriate method to achieve the stoppage reactions in AAS pastes.

^{1}H-^{29}Si solid-state CPMAS NMR and ^{29}Si MAS NMR spectra were acquired on an Agilent VNMRS Direct Drive 400 MHz spectrometer (9.4 Tesla) equipped with a T3HX 3.2 mm probe. The signal of talc for both two types of NMR tests was used to calibrate the silicon chemical shift scale (-98 ppm). Magic angle spinning was performed at 8 kHz and 6.5 kHz using ceramic zirconia rotors for ^{1}H-^{29}Si CP MAS NMR and ^{29}Si MAS NMR test, respectively. Acquisition parameters in ^{1}H-^{29}Si CP MAS

NMR (or ^{29}Si MAS NMR) used were: a spectral width of 24 kHz, a 90° pulse length of 3.2 μs (or 4.5 μs), an acquisition time of 15 ms, a recycle delay time of 3 s (or 20 s), a spin-lock field of 80 kHz, a contact time of 1 ms (or a recycle delay time of 20 s), and about 100000 accumulations (or about 8000 accumulations). High-power proton dipolar decoupling during the acquisition time for both two types of NMR tests was set to 80 kHz. The spectra of ^{1}H-^{29}Si CPMAS NMR and ^{29}Si MAS NMR were decomposed by the Gaussian peaks, and the specified full width at half height was always less than 10 ppm [24].

2.3.6 Scanning electron microscopy of AAS pastes

SEM with secondary electron mode were used to observe the morphology of AAS pastes. The stoppage method of the reactions was elucidated in the previous section. The specimens at different reaction times were carbon coated before imaging.

3. Results and discussions

3.1 Structural build-up behavior and initial setting times of AAS pastes.

Fig. 3a presents the evolution of the early storage modulus of AAS pastes activated by sodium hydroxide and sodium silicate. As seen in Fig. 3a, these two mixtures exhibited completely different structural build-up behavior. The increase of structural build-up of sodium hydroxide-activated slag paste started off with a greater storage modulus, followed by a steadily rising rate of structural build-up over time. The trend of the structural build-up behavior is quite similar to that of Portland cement. Previous studies have reported that a sharp increase in the storage modulus is observed in the first 30 min for Portland cement due to the formation of the percolated network [9], [10], [25]. After that, the storage modulus increases at a relatively lower rate, indicating the sequential development of hydration products at cement particle contact locations [9]. Due to the high alkaline environment for the mixture NH-AAS, the rapid reaction rate of GGBFS could also enhance the formation of reaction products, furthermore inducing the occurrence of the percolated network [6]. In the meantime, the rapid reaction product formation could cover slag's surface, preventing further slag reaction [7].

Therefore, a continuous increase in the storage modulus of NH-AAS could be observed. It could then be considered that the setting process of NH-AAS follows a similar mechanism as that of Portland cement [20].

However, the evolution of the structural build-up of SS-AAS was significantly different from the case of NH-AAS. The initial storage modulus started from a very low value as compared to NH-AAS. In the first 20 min, almost no structural formation could be observed for the mixture SS-AAS. However, afterwards, the storage modulus of SS-AAS steeply increased. Some researchers attribute the very low initial storage modulus of SS-AAS to the viscous nature of sodium silicate solution with a great number of aqueous silicates, which prevents the formation of the percolated network [10], [26]. The mild alkaline environment provided by the sodium silicate solution allowed a considerable time to dissolve GGBFS, providing sufficient calcium and aluminum. Once these ions reach their critical concentration, they will interact with the silicates originated from the activator solution, significantly leading to a significantly larger number of reaction products in the matrix [7], [10], [12]. Therefore, a rapid increase in storage modulus could be observed for the SS-AAS mixtures. It should be noted here that the initial setting times of AAS pastes were also consistent with the trend of the structural build-up. The mixture of SS-AAS showed a short initial setting (45 min) as compared to that of NH-AAS (120 min).

Fig. 3b presents the evolution of loss factor of NH-AAS and SS-AAS mixture. In first 20 min, the loss factor for NH-AAS mixture decreased dramatically, afterwards, the downward trend started to slow down until the loss factor dropped to 0, reflecting that the paste reached solid-like state at around initial setting time (120 min). By contrast, mixture SS-AAS showed an inverse trend. The loss factor for mixture SS-AAS decreased slowly in the first 20 min, indicating its more viscous behavior. Then, a rapid decrease could be observed for SS-AAS mixture until its initial setting time (45 min). This showed that SS-AAS mixture reached solid-like state earlier than NH-AAS mixture.

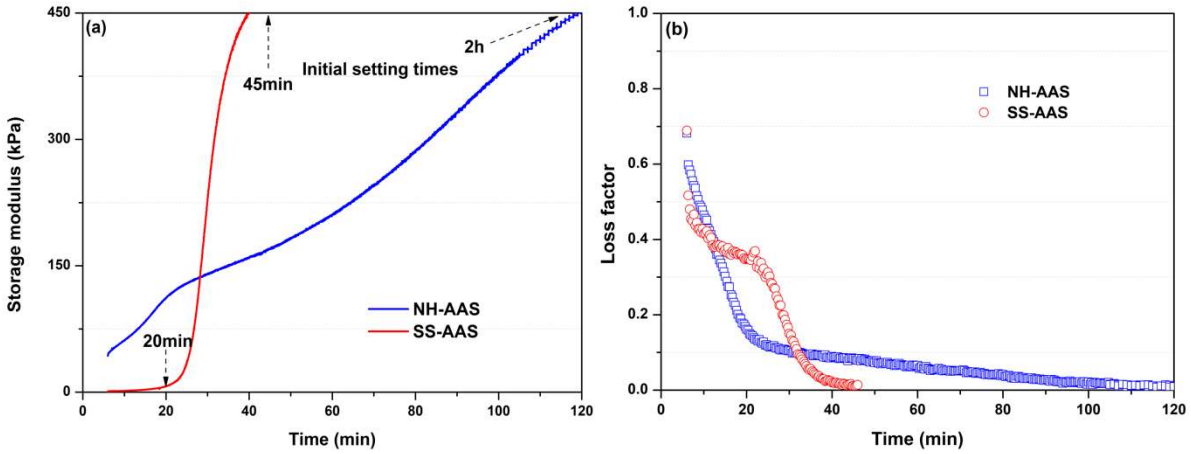

Fig. 3. Evolution of storage modulus (a) and loss factor (b) of sodium hydroxide-activated and sodium silicate-activated GGBFS pastes.

3.2 Calorimetric investigation of AAS pastes.

The evolution of calorimetric curves, including heat flow and cumulative heat release of AAS pastes, is presented in Fig. 4. As well known, there are five distinct stages for the AAS mixtures: dissolution, induction, acceleration, deceleration and steady-state [29]–[32]. As demonstrated in Fig. 4a, the AAS mixtures exhibited a high local peak during the first 20 min. Rapid heat evolution was observed when the activator solution was in contact with GGBFS, being mostly related to the wetting and dissolution of GGBFS particles and partly related to the interaction of silicate units and sodium with calcium and aluminum dissolved from GGBFS [33], [34]. For SS-AAS pastes, the dissolution stage was followed by an induction period in the heat flow, while no such period was seen for the NH-AAS pastes. The observed acceleration peak (second peak) after the induction period for the AAS pastes is usually associated with the onset of the main strength and microstructural development [35]. The occurrence of the acceleration peak of SS-AAS was delayed as compared to the NH-AAS mixture, and the intensity of the acceleration peak in the SS-AAS was lower as compared to the NH-AAS mixture, which is also consistent with previous studies [29], [33]. This could be related to the lower pH value of the sodium-silicate activator solution compared to the sodium-hydroxide activator (Table 2). It was reported that the higher alkaline environment normally enhances the dissolution rate and slag reaction degree [36]. Additionally, increasing alkalinity also improves the solubility of silica and alumina in solution, which could induce more reaction product formation [27], [37].

The cumulative heat release of NH-AAS showed a higher value as compared to that of SS-AAS at the age of 72 h. However, in the first 3.5 h, the SS-AAS released more heat than NH-AAS. This is probably due to the interaction between the calcium ions, continuously released from GGBFS, and the silicate ions, originating from sodium silicate solution, quickly forming large amounts of gel products [38]. This is also consistent with the rapid increase in storage of SS-AAS in the early time. On the other hand, NH-AAS and SS-AAS both presented a similar cumulative heat release of around 17 J/g at their initial setting times (Fig. 4b).

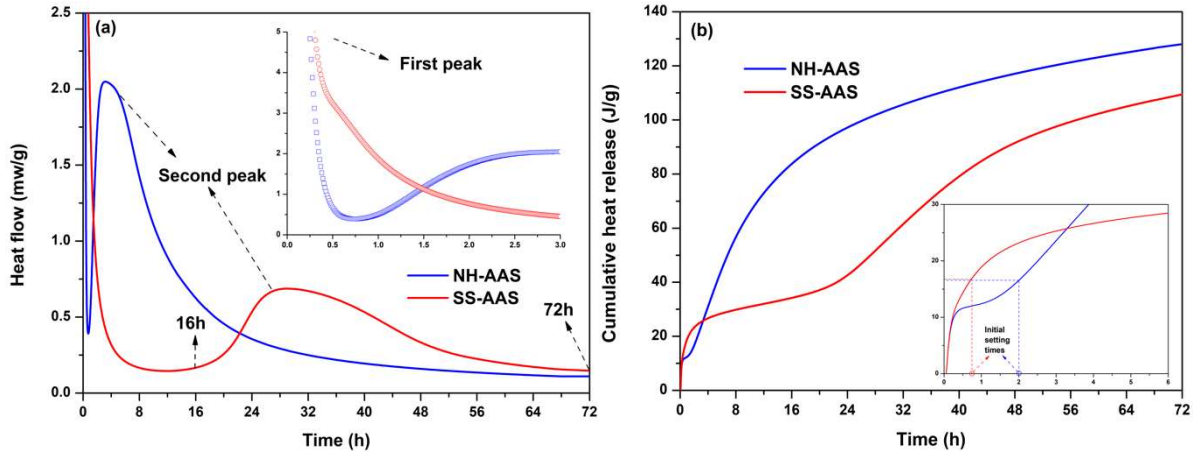

Fig. 4. Evolution of heat flow (a) and cumulative heat release (b) of sodium hydroxide-activated and sodium silicate-activated GGBFS pastes.

3.3 NMR analysis of AAS pastes

To further understand the relationships between the nanostructure and the setting process of AAS, NMR tests were carried out on the samples taken at critical reaction times based on storage modulus, setting time and calorimetric measurements. Three samples were taken at 20 min and 45 min (initial setting time, as shown in Table 2) for the SS-AAS mixture and at 120 min (initial setting time) for the NH-AAS mixture based on storage modulus and setting times as shown in Fig. 3. In addition, two samples were taken from the SS-AAS mixture corresponding to the beginning of the acceleration stage (16 h) and the end of the deceleration period (72 h), based on the calorimetry measurements as shown in Fig. 4.

278 *3.3.1 NMR analysis at initial setting times*

279 The ^{29}Si MAS NMR spectra of the anhydrous GGBFS and the pastes at different reaction times are
280 given in Fig. 5. As shown in Fig. 5, the anhydrous slag was the primary source of the signal at -76.8
281 ppm in all the spectra. In addition, a shoulder between -80 and -105 ppm was observed at the initial
282 setting time for NH-AAS (120 min) and SS-AAS mixtures (45 min), reflecting the reaction product
283 formation. Therefore, these reaction products should be responsible for the initial setting of AAS. No
284 difference was observed between the spectra of SS-AAS_20min and anhydrous GGBFS, indicating no
285 reaction product formation at 20 min. This was also consistent with the results of the structural build-
286 up of the SS-AAS mixture, showing no significant structural formations at 20 min.
287
288 To better understand the nanostructure of AAS, an accurate deconvolution should be performed on the
289 shoulder region. However, since some Q^n (mAl) (n=0,1,2,3,4 and m=0,1,2,3,4) peaks were overlapped
290 in the ^{29}Si MAS NMR spectra [39], a ^{1}H-^{29}Si CPMAS NMR test was performed to find the peak
291 positions, prior to the deconvolution of ^{29}Si MAS NMR spectra. It should be noted that the chemical
292 shift of each resonance is required to be consistent in both the ^{29}Si MAS NMR and ^{1}H-^{29}Si CPMAS
293 NMR spectral deconvolutions.
294
295 Fig. 6 and Fig. 7 present the differences between the ^{1}H-^{29}Si CPMAS NMR and ^{29}Si MAS NMR
296 spectra of the pastes activated by sodium hydroxide and sodium silicate, respectively, as well as their
297 detailed deconvolution. The resonances observed in the ^{1}H-^{29}Si CPMAS NMR are influenced by their
298 proximity to protons and the Hartmann-Hahn contact period, and so this spectrum particularly shows
299 those Si species present in the hydration reaction products [40]. As a result, the ^{1}H-^{29}Si CPMAS NMR
300 data in Fig. 6 and 7 can confirm that the broad resonance feature observed in the ^{29}Si MAS NMR is
301 highly due to the presence of the anhydrous slag in the AAS. It should be noted that although the ^{1}H-
302 ^{29}Si CPMAS NMR can provide better resolution of the spectra in terms of reaction products, it can
303 only give qualitative information rather than quantitative information. Therefore, the combined use of
304 ^{1}H-^{29}Si CPMAS NMR and ^{29}Si MAS NMR enables a more complete examination of the variations in
305 the nanostructure of reaction products that are formed in the AAS mixtures.

The nanostructure of AAS can be identified by the $Q^n(mAl)$ structural units, showing various chemical environments of silicon tetrahedral of phases in ^{29}Si NMR spectra, where n denotes the number of oxygen bridges between each silicon tetrahedral unit and other silicon atoms, and m represents the number of aluminum tetrahedral occupying bridging positions [41], [42]. The deconvolution results of the $Q^n(mAl)$ structural units in the ^{29}Si MAS NMR spectra are summarized in Table 3. The deconvoluted peak located around -76.8 ppm for NS-AAS and SS-AAS mixtures at initial setting times refers to the remnant GGBFS (Q^0), and the integration of these peaks reached 80.04% and 81.28% of the spectra of ^{29}Si MAS NMR, respectively. In other words, when both NH-AAS and SS-AAS mixtures show an initial setting, they both have a similar reaction degree. Therefore, it may indicate that the initial setting of AAS would occur when the reaction degree of GGBFS approached 20%. Combining the results of rheology and setting time, it can be concluded that the solidification of NH-AAS is a continuous process; however, the initial set of SS-AAS occurs suddenly in a shorter period [20].

As shown in Fig. 6b, the peak position for the mixture NH-AAS_120 min with δ = -79.2 is attributed to the Q^1 site, which is a terminal silicate tetrahedral site inside C-A-S-H gels [24], [43]. The middle-of-chain silicate inside C-A-S-H gels is connected to the $Q^2(1Al)$ and Q^2 sites at -83.5 ppm and -86 ppm, respectively [41], [44]. Since there is an overlap between resonances in this region, the peak at -89.2 ppm belongs to $Q^3(1Al)$ and $Q^4(4Al)$ sites [16], [24], [45]. Herein, it should be noted that the $Q^3(1Al)$ site denoted a substantial degree of cross-linking with the C-(N-)A-S-H gel [24], [40], while $Q^4(4Al)$ site refers to the Al-rich N-A-S-H gel [46]. Additionally, $Q^4(2Al)$, $Q^4(1Al)$, and $Q^4(0Al)$ each have their own set of three extra sites located somewhere in the range of -96 to -110 ppm. The $Q^4(mAl)$ environments are attributed to a polymerized Si-rich N-A-S-H gel [12], [40], [47].

Similarly, as shown in Fig. 7b, three resonances with δ = -78.5 ppm, -83.0 ppm and -86 ppm, are attributed to Q^1, $Q^2(1Al)$ and Q^2 sites, respectively, indicating the formation of C-A-S-H in the SS-AAS mixture. The $Q^3(1Al)$ and $Q^4(4Al)$ sites are located at -88.6 ppm, showing the formation of high

crosslinking C-(N-)A-S-H and N-A-S-H, respectively. In addition, the alumino-silicate gel N-A-S-H can be confirmed by three additional peaks between -93 and -106 ppm, indicating the Q^4(3Al), Q^4(2Al) and Q^4(1Al) sites, respectively.

As shown in Table 3, it is found that the SS-AAS mixture showed a higher percentage of N-A-S-H formation (Q^4(mAl)) as compared to C-A-S-H (Q^1, Q^2(1Al) and Q^2), while the amount of C-A-S-H (Q^1, Q^2(1Al) and Q^2) was more than N-A-S-H (Q^4(mAl)) in the NH-AAS mixture. Although it was very difficult to distinguish the net amounts of Q^3(1Al) and Q^4(4Al) due to their overlapped resonance, it could still be concluded that the SS-AAS mixture contained a higher percentage of N-A-S-H as compared to the NH-AAS mixture at initial setting times based on the other Q species. In addition, it is well known that the sodium silicate solution contains high Q species [13], [17]. Due to the condensed silicates in the activator of SS-AAS, these higher-Q Si species are more likely to condense with Al and Ca to form 3D Ca-modified gel at early ages [48], [49]. While regarding the NaOH-activated mixture, congruent dissolution of the various Si coordination environments in the precursors is highly unlikely to occur during alkali activation due to the presence of many phases in the precursors and the previously observed preference of Al over Si dissolution in the silicoaluminate precursors. Furthermore, the highly polymerized aluminosilicate phase is predicted to disintegrate more slowly than the depolymerized calcium silicate phases observed in the precursors [46], [50]. And these released depolymerized silicates interacted with aluminum and calcium ions to form chain-like C-A-S-H gel [15], [37]. This could be the reason for the distinctive difference between SS-AAS and NH-AAS in terms of gel composition at early ages.

It is plausible to see that the hydration products of AAS at initial setting times are composed of the C-A-S-H and N-A-S-H gels. In the meantime, the coexistence of C-A-S-H and N-A-S-H resulted in a 3D Ca-modified gel (N,C)-A-S-H, which was also reported by Garcia-Lodeiro et al. [51]. However, very few studies have focused on the gel composition of AAS at the initial setting time in the literature. Only Palacios et al. [12] used the thermodynamic modeling and NMR technique to confirm the presence of the coexisting formation of the alumino-silicate gel and C-A-S-H gel in the sodium

362 silicate-activated slag mixtures at early times. These C-A-S-H and N-A-S-H gels are formed from the
363 reactions of Ca^{2+} ions and aluminate species dissolved from slag and Na^{+} and silicate species initially
364 existed in the solution. Therefore, the rheological properties and the setting process are determined by
365 these reaction products.
366
367 However, many studies, in general, pointed out that the main reaction products of AAS at later ages
368 are C-A-S-H gels. It is, therefore, very worthwhile to investigate when these N-A-S-H gels start to
369 disappear or whether they are converted into C-A-S-H gels as the reaction continues. Therefore, to
370 investigate a possible change in the gel composition of AAS at an early time, NMR tests were
371 conducted on the samples taken at two critical reaction times based on the isothermal calorimetric
372 curves of SS-AAS pastes (as shown in section 3.4.2).
373

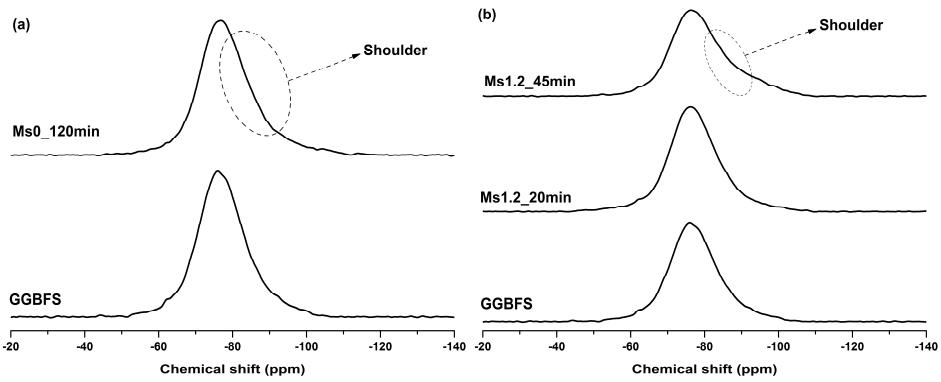

374
375 Fig. 5. The original ^{29}Si MAS NMR spectra of AAS, (a) NH-AAS, (b) SS-AAS.
376
377
378

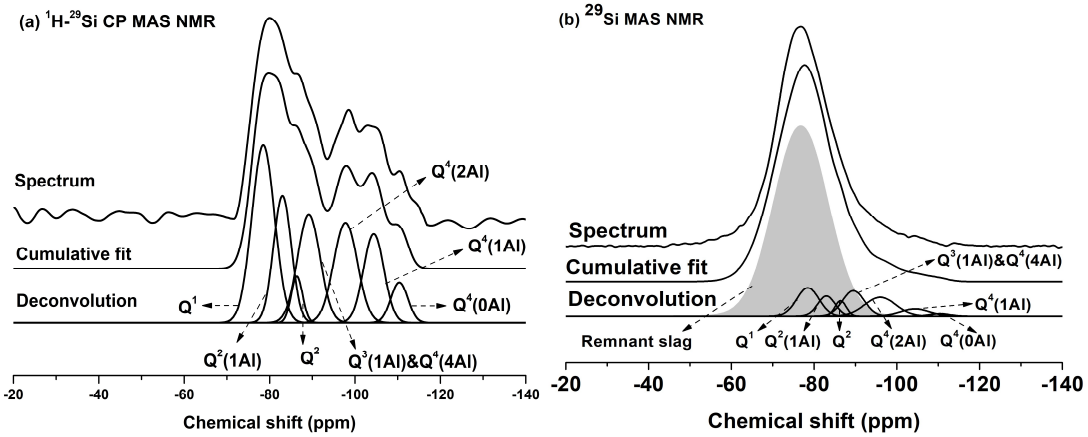

Fig. 6. The deconvolution of ^{1}H-^{29}Si CPMAS NMR and ^{29}Si MAS NMR spectra of NH-AAS at initial setting time (120 min), (a) The deconvolution of ^{1}H-^{29}Si CPMAS NMR, (b) The deconvolution of ^{29}Si MAS NMR.

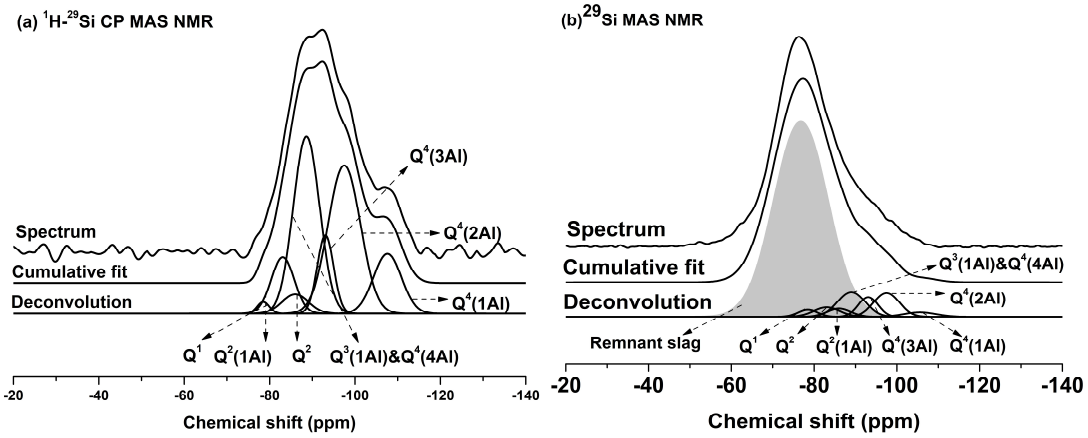

Fig. 7. The deconvolution of ^{1}H-^{29}Si CPMAS NMR and ^{29}Si MAS NMR spectra of SS-AAS at the initial setting time (45 min), (a) The deconvolution of ^{1}H-^{29}Si CPMAS NMR, (b) The deconvolution of ^{29}Si MAS NMR.

Table 3. The deconvolution results of the ^{29}Si MAS NMR spectra of AAS mixtures over time based on area percentage (%).

Mixtures	Unreacted slag	Reaction Products							
		C-A-S-H/C-(N-)A-S-H					N-A-S-H		
	Q^0	Q^1	Q^2(1Al)	Q^2	Q^3(1Al) &Q^4(4Al)	Q^4(3Al)	Q^4(2Al)	Q^4(1Al)	Q^4(0Al)
NH-AAS_120min	80.04 (-76.8 ppm)	4.93 (-78.5 ppm)	2.74 (-83.0 ppm)	1.34 (-86.4 ppm)	4.38 (-89.3 ppm)	-	4.59 (-96.5 ppm)	1.62 (-104.4 ppm)	0.38 (-110.4 ppm)
SS-AAS_45min	81.28 (-76.8 ppm)	1.07 (-78.5 ppm)	1.93 (-83.1 ppm)	1.51 (-86.0 ppm)	5.32 (-89.0 ppm)	2.99 (-93.1 ppm)	4.75 (-97.2 ppm)	1.14 (-105.6 ppm)	-
SS-AAS_16h	68.68 (-76.8 ppm)	2.45 (-78.5 ppm)	3.80 (-83.1 ppm)	4.65 (-86 ppm)	7.63 (-88.9 ppm)	5.34 (-93.1 ppm)	4.85 (-97.3 ppm)	2.60 (-105.6 ppm)	-
SS-AAS_72h	48.46 (-76.8 ppm)	18.22 (-78.8 ppm)	13.58 (-83.6 ppm)	8.09 (-86.2 ppm)	5.55 (-89.1 ppm)	3.68 (-93.6 ppm)	2.42 (-97.5 ppm)	-	-

3.3.2 NMR analysis of SS-AAS pastes based on calorimetric curves

Fig. 8 illustrates the ^{29}Si MAS NMR of SS-AAS pastes over time. As the curing age increased from the beginning to 16 h, the broad peak did not shift significantly, while the shoulder area between -80 and -105 ppm was enhanced. With time elapsing from 16 h to 72 h, the broad peak started to shift to a higher value, and the shoulder area between -90 and 105 ppm significantly decreased. This is possibly due to the increase of polymerization degree and cross-linking of gels over time and the disappearance of the alumino-silicate gel.

^{29}Si MAS NMR decomposition results of the SS-AAS mixture at around the starting time of the acceleration peak and the end of the deceleration peak observed in the isothermal calorimetric curves are presented in Fig. 9. The area percentage of various Q^n(mAl) structural units are quantified and summarized in Table 3. As can be seen from Fig. 9, Q^2(1Al) and Q^2 sites within C-A-S-H increased from 3.80 % to 13.58 % and from 4.65 % to 8.09 % with increasing curing time from 16 h to 72 h, respectively. In particular, the content of Q^1 significantly increased from 2.45 % to 18.22 % with time elapsing and became the most dominant Q^n(mAl) structural unit in SS-AAS pastes at the age of 72 h. This is also consistent with the previous studies, reporting the dissolved calcium and aluminum from slag enhance the gel polymerization and result in more crosslinked C-A-S-H gels [24]. During the proceeded reaction time from the initial setting time (45 min) to 16 h and then to 72 h, the content of Q^3(1Al) & Q^4(4Al) gradually increased from 5.32 % to 7.63 % and then decreased to 5.55 %. Meanwhile, the content of N-A-S-H gel (including Q^4(mAl), m=3, 2, 1, 0) first increased from 8.88 % to 12.79 % when the age increased from 45 min to 16 h and then decreased to 6.10 % when the age increased from 16 h to 72 h. This indicates that the system is continuously enriched with N-A-S-H until the end of the induction period; however, as the reaction proceeded, the N-A-S-H started to destabilize to form C-A-S-H when reaching the end of the second exothermic peak of SS-AAS.

Based on the NMR results in this study and the compatibility between C-A-S-H and N-A-S-H gels [51], the activation process of SS-AAS pastes in the early times can be explained as follows. After mixing the GGBFS with sodium silicate solution, the process begins with the dissolution of the GGBFS particles in the alkaline solution via rupture of the T-O-T bonds (T: Si or Al) and Ca-O bonds in the slag, resulting in a wide variety of dissolved species. This can be confirmed by various previous studies, which use ICP-OES to observe the change of different ion concentrations [6], [7], [13], [15], [27], [37]. When the ions reach their oversaturation, a great number of C-A-S-H and N-A-S-H gels precipitate. These gels generally contain a high aluminum content, as shown in the NMR results in this study. As the alkaline reaction proceeds, the silicates from the original activator solution are consumed during the formation of reaction products. Therefore, the Si-O bonds in GGBFS start to dissolve and keep the silicon concentration at a high level. In this study, from the initial setting time to 16 h, Si

435 uptake enhances the gel condensation in terms of C-A-S-H, leading to an increase in Q^2(1Al). In the
436 meantime, the percentage of N-A-S-H gel also increases when the age increases from the initial setting
437 time to 16 h.
438
439 Additionally, with time elapsing, the calcium and aluminum ions in the aqueous solution begin to
440 diffuse throughout the cementitious matrix and a certain level of Ca ions reacts with N-A-S-H to form
441 (N,C)-A-S-H. Since calcium and sodium ions have the same ionic radius and electronegative potential,
442 the 3D structure of the (N,C)-A-S-H type gel is maintained by an ion exchange process, in which
443 calcium can replace the sodium ions in a mechanism similar to that observed in clay and zeolites [52].
444 When calcium concentrations are high enough, they diffuse into pores in the matrix and interact with
445 the (N,C)-A-S-H gel. Because of the Ca^{2+} polarising effect, the Si-O-Al bonds are under tension and
446 eventually broken, forming Si-O-Ca bonds. As aluminum is released from the N-A-S-H gel, fewer
447 polymerized structures, such as C-A-S-H gels, are formed. Simultaneously, the C-A-S-H gel formed in
448 earlier phases is capable of absorbing a significant amount of silicon and aluminum ions in bridge
449 positions [53]. Besides, Puertas et al. [15] also found that the calcium concentration and pH value of
450 the waterglass-activated slag mixtures reached a peak value at the age of 24h. This also supports that
451 the N-A-S-H gel will degrade to C-A-S-H due to its low stability in the presence of high pH and high
452 calcium concentrations, as reported by Garcia-Lodeiro et al. [51]. Eventually, the chain-like C-A-S-H
453 gels will form and dominate the reaction products, which is also consistent with this study where Q^1
454 Q^2 and Q^2(1Al) are the main Q species at the age of 72h.

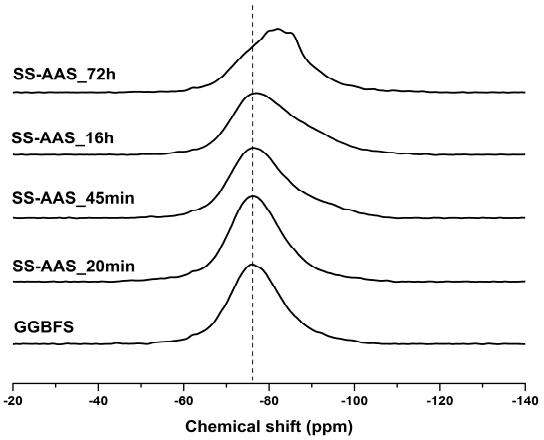

455

456 Fig. 8. The ^{29}Si MAS NMR spectra of anhydrous GGBFS and SS-AAS pastes at different times.

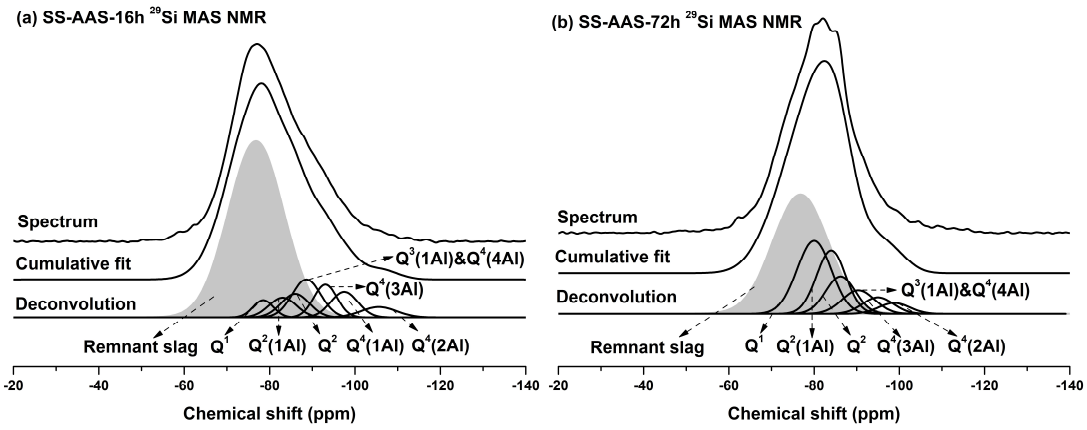

Fig. 9. The deconvolution of ^{29}Si MAS NMR spectra of SS-AAS at around: (a) starting point of the acceleration period (16 h) and (b) at the end of the deceleration period (72 h) based on isothermal calorimetric curves.

3.3.3 Quantitative assessment of C-A-S-H/C-(N-)A-S-H and N-A-S-H

Fig. 10 presents the deconvolution results for the ^{29}Si MAS NMR spectra of the SS-AAS mixture over time. It could be seen that in the first 16 h, the Q^4(mAl) is dominated as compared to other Q^n environments. As curing time proceeded, the Q^4(mAl) started to decrease, in particular for the Q^4(1Al), which decreased to zero at 72 h. However, other chain-like Q^n increased.

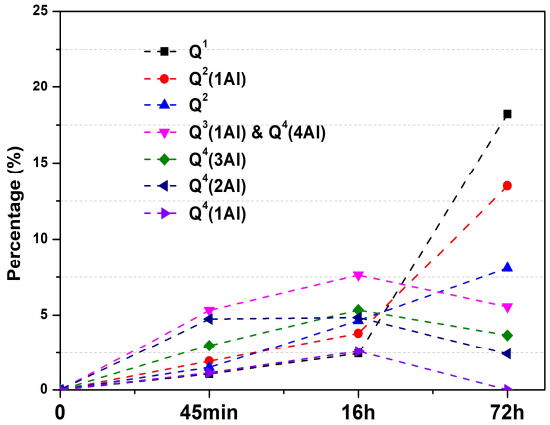

Fig. 10. The deconvolution results for the ^{29}Si MAS NMR spectra of SS-AAS mixture over time.

Richardson and Groves [54] have proposed a conceptual model named “substituted general model” (SGM) to describe the C-(N-)A-S-H product, which is a mixture of 14 Å tobermorite, jennite, and $Ca(OH)_2$ structures. However, in recent studies, more formation of cross-linked Si sites, such as Q^3 and Q^3(1Al), is identified by the

high-resolution ^{29}Si MAS NMR [24], [36], [39], [41]. As reported by Myers et al. [24], in tobermorite structural models, Q^3-type silica bonding environments can only be described by cross-linking between bridging sites in the silicate chains. Therefore, another conceptual model, the "Cross-linked substituted tobermorite model" (CSTM), has been proposed to support the description of the C-(N-)A-S-H gel as a mixture of cross-linked (11 Å tobermorite) and non-cross-linked (14 and/or 9 Å tobermorite) chains. And it should be noted that there are some structural constraints included in the CSTM model: (i) two times as many silicate species exist in the form (Q^2 + Q^2(1Al)) as in the form (Q^3 + Q^3(1Al) + Al[4]). (ii) since aluminum is only substituted into bridging sites in cross-linked tobermorite, the fraction of aluminum substitution into Q^3 type sites is equal to the ratio of Q^2(1Al) to Q^2 sites, and (iii) the introduction of one Al[4] species into cross-linked tobermorite introduces one Q^3(1Al) and two Q^2(1Al) Si species. Regarding the structure of N-A-S-H, unfortunately, no acknowledged conceptual model has been proposed due to its complicated 3D structures.

To further investigate the structure of the investigated samples in this study, two extreme scenarios are considered. In this study, as the Q^3(1Al) and Q^4(4Al) are overlapped at around -89 ppm, it was assumed as a first case that all the signals came from Q^4(4Al) and there was no Q^3(1Al) in the nanostructure, which means all C-(N-)A-S-H structures consist of non-cross-linked gel as defined by the SGM model. In the second extreme case, it was assumed that the C-(N-)A-S-H had the maximum crosslinking degree (maximum content of Q^3(1Al), and the remaining part is Q^4(4Al)), considering the abovementioned structural constraints. This indicates that the C-(N-)A-S-H is a mixture of cross-linked and non-cross-linked tobermorite-like structures as defined by CSTM.

Table 4 presents the C-A-S-H/C-(N-)A-S-H and N-A-S-H gel amounts considering the two extreme scenarios above. As shown in Table 4, the calculated amounts of C-A-S-H/C-(N-)A-S-H and N-A-S-H vary in a narrow band for these two extreme scenarios except the mixture SS-AAS_72h. For example, NH-AAS_120 min exhibited a range of C-A-S-H/C-(N-)A-S-H between 9.01 and 9.68, and N-A-S-H was between 10.30 and 10.97. In both scenarios, the relative amount of C-A-S-H/C-(N-)A-S-H is closer to N-A-S-H gel for the mixture of NH-AAS_120 min, while the N-A-S-H gel is much more dominant in the mixture of SS-AAS_45 min. With time elapsing, the C-A-S-H/C-(N-)A-S-H amount increased rapidly, while the amount of N-A-S-H firstly increased until the end of the induction period based on calorimetric curves. At the end of deceleration period based on calorimetric curves (72h), the N-A-S-H formation for mixture SS-AAS decreased significantly for both two extreme scenarios as compared to the mixture at the age of 16h.

Table 4 Nanostructure of investigated pastes in this study considering the two extreme scenarios.

	Mixture	Q^1	Q^2(1Al)	Q^2	Q^3(1Al)	Q^4(4Al)	Q^4(3Al)	Q^4(2Al)	Q^4(1Al)	Q^4(0Al)	C-A-S-H/C-(N-)A-S-H	N-A-S-H
No cross-link in C-A-S-H/C-(N)-A-S-H	NH-AAS_120min	4.93	2.74	1.34	-	4.38	-	4.59	1.62	0.38	9.01	10.97
	SS-AAS_45min	1.07	1.93	1.51	-	5.32	2.99	4.75	1.14	-	4.51	14.20
	SS-AAS_16h	2.45	3.80	4.65	-	7.63	5.34	4.85	2.60	-	10.90	20.42
	SS-AAS_72h	18.22	13.58	8.08	-	5.55	3.68	2.42	-	-	39.88	11.65
Maximum cross-link in C-A-S-H/C-(N)-A-S-H	NH-AAS_120min	4.93	2.74	1.34	0.67	3.71	-	4.59	1.62	0.38	9.68	10.30
	SS-AAS_45min	1.07	1.93	1.51	0.27	5.05	2.99	4.75	1.14	-	4.78	13.93
	SS-AAS_16h	2.45	3.80	4.65	0.61	7.02	5.34	4.85	2.60	-	11.51	19.81
	SS-AAS_72h	18.22	13.58	8.08	4.04	1.51	3.68	2.42	-	-	43.92	7.61

3.4 SEM images of AAS pastes

Scanning electron microscopy (SEM) was used to evaluate the surface morphology development of the AAS pastes [12], [16]. Fig. 13 presents SEM images of AAS pastes during the reaction process. At the age of 120 min for NH-AAS (Fig. 13c and 13d) and 45 min for SS-AAS (Fig. 13g and 13h), the GGBFS particle surfaces became rough due to the precipitation of reaction products, thereby probably leading to the initial set of AAS pastes.

As shown in Fig. 13e and 13f, the surface of the GGBFS particles of the SS-AAS mixture at the age of 20 min was very smooth, indicating no detectable reaction product formation at this age. This is also consistent with the structural build-up and NMR results in this study. With time elapsing, the dissolved calcium and aluminum ions from the GGBFS reached oversaturation and interacted with the silicates originating from the activator solution, forming more reaction products. Therefore, the surface of GGBFS particles became increasingly rough, and more particles would connect to each other due to the formation of reaction products (as shown in Fig. 13k and 13l) [12].

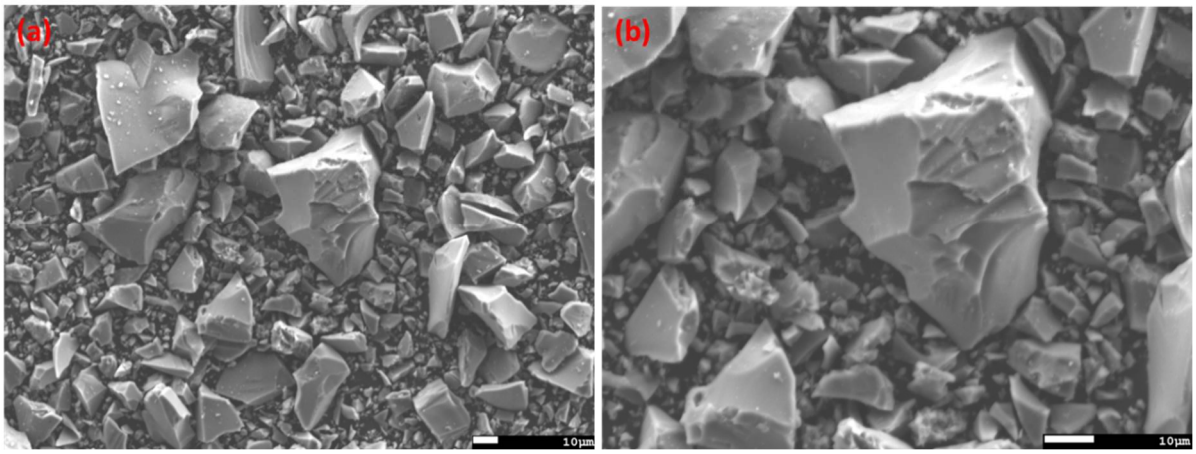

Original GGBFS

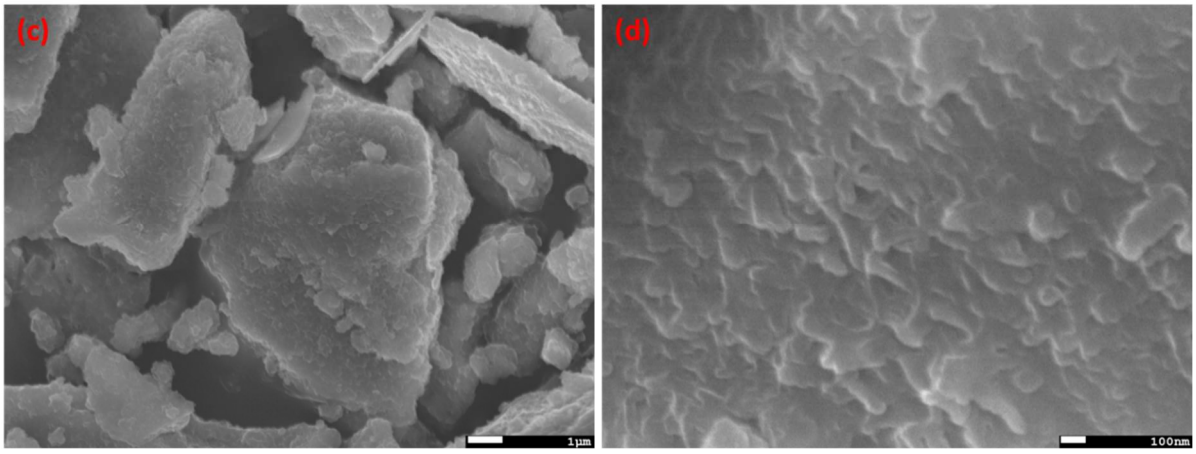

NH-AAS_120min

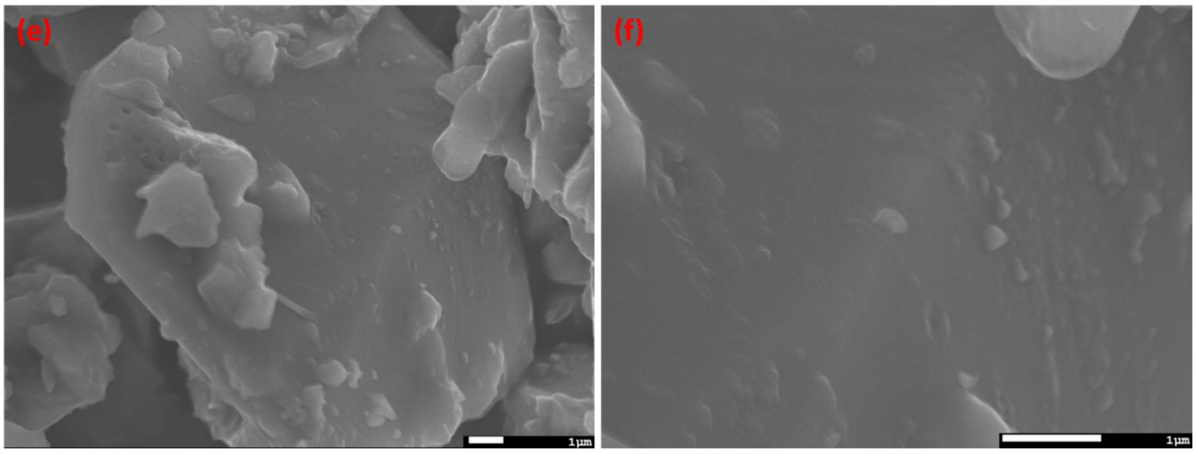

SS-AAS_20min

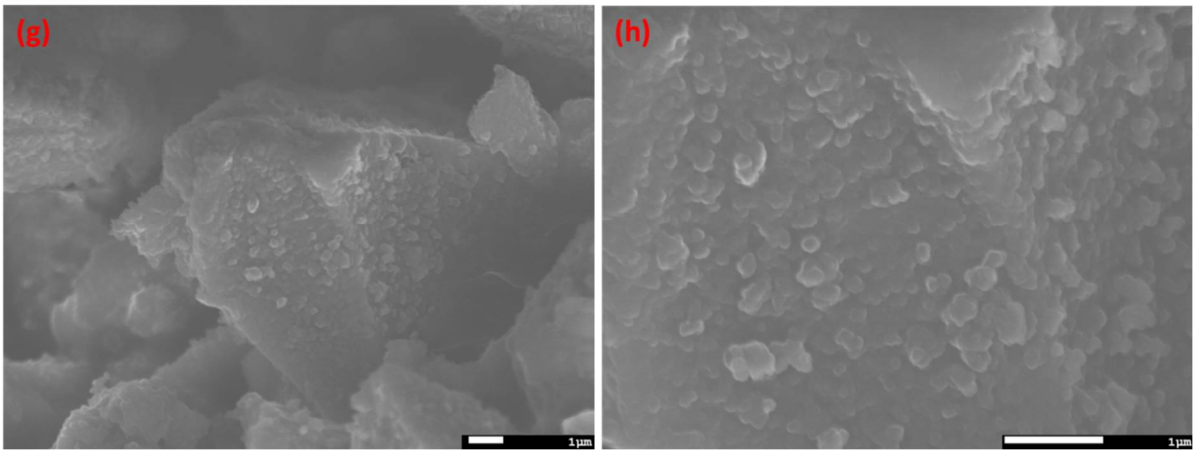

SS-AAS_45min

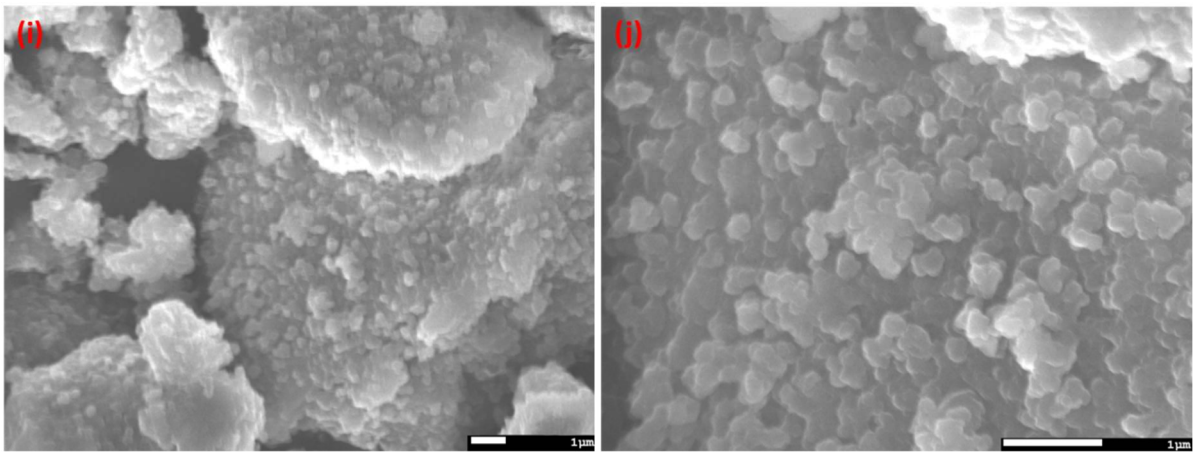

SS-AAS_16h

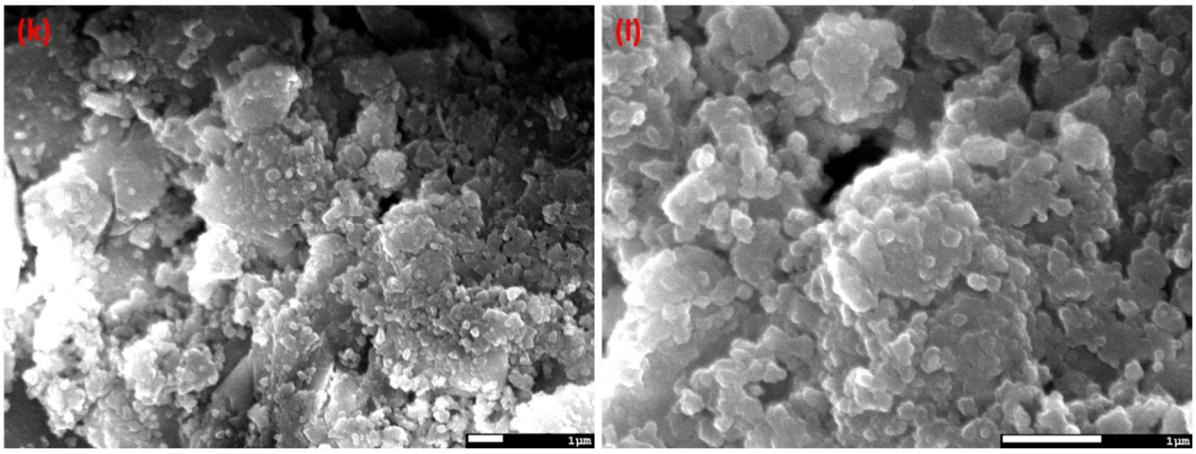

SS-AAS_72h

Fig. 13. SEM images of AAS pastes over time; (a, b) anhydrous GGBFS; (c, d) NH-AAS at 120 min; (e, f) SS-AAS at 20 min; (g, h) SS-AAS at 45 min; (i, j) SS-AAS at 16 h; (k, l) SS-AAS at 72 h.

4. Conclusions

Following are the primary conclusions that can be derived from the experimental findings:

- The NH-AAS reaches its initial setting time with a long, continuously proceeding structuration process. On the contrary, SS-AAS reaches its initial setting with an abrupt increase in the structuration process. At their initial setting times, the NH-AAS and SS-AAS mixtures release similar heat and reach a similar reaction degree.
- At initial setting times, the C-A-S-H and N-A-S-H gels are both formed in the NH-AAS and SS-AAS mixtures. The difference, however, is that the amount of C-A-S-H gel is relatively similar to N-A-S-H gel in NH-AAS, while SS-AAS contains much more N-A-S-H gel.
- With time elapsing, more N-A-S-H gel in the SS-AAS mixture precipitates up to the end of the induction period. However, the 3D N-A-S-H gel degrades to a chain-like C-A-S-H gel after the acceleration peak recorded in the isothermal calorimetric curves.

The findings presented in this study can help researchers understand, to some extent, the early gel composition and alkaline activation process of AAS mixtures. However, some remaining challenges still need to be addressed in further research. For example, modeling the N-A-S-H structure could help understand the reaction process. In addition, more research on the relationships between the composition factors and inter-particle forces could also help better understand the interaction mechanisms before setting times.

Authorship contribution statement

Xiaodi DAI: Methodology, Conceptualization, Investigation, Writing – original draft; **Serdar AYDIN**: Methodology, Conceptualization, Writing – review editing; **Mert Yücel YARDIMCI**: Methodology, Validation, Writing – review editing; **Gunter REEKMANS**: Investigation, Validation; **Peter ADRIAENSENS:** Investigation, Validation; **Geert De SCHUTTER**: Funding acquisition, Supervision, Writing - review & editing.

Acknowledgement

This paper is a scientific output of the research actions performed in the framework of the FWO-EOS project 30439691 'INTERdisciplinary multiscale Assessment of a new generation of Concrete with alkali-activated maTerials' (INTERACT). The financial support by FWO-EOS is gratefully acknowledged. The NMR work is supported by Hasselt University and the Research Foundation Flanders (FWO Vlaanderen) via the Hercules project AUHL/15/2 - GOH3816N).

Reference

[1] RILEM-TC 224-AAM, *Alkali Activated Materials*. 2014.

[2] J. L. Provis and S. A. Bernal, "Geopolymers and Related Alkali-Activated Materials," *Annu. Rev. Mater. Res.*, vol. 44, no. 1, pp. 299–327, 2014, doi: 10.1146/annurev-matsci-070813-113515.

[3] C. Shi, B. Qu, and J. L. Provis, "Recent progress in low-carbon binders," *Cem. Concr. Res.*, vol. 122, no. May, pp. 227–250, 2019, doi: 10.1016/j.cemconres.2019.05.009.

[4] S. K. Nath and S. Kumar, "Reaction kinetics, microstructure and strength behavior of alkali activated silico-manganese (SiMn) slag – Fly ash blends," *Constr. Build. Mater.*, vol. 147, pp. 371–379, 2017, doi: 10.1016/j.conbuildmat.2017.04.174.

[5] S. A. Bernal and J. L. Provis, "Durability of alkali-activated materials: Progress and perspectives," *J. Am. Ceram. Soc.*, vol. 97, no. 4, pp. 997–1008, 2014, doi: 10.1111/jace.12831.

[6] X. Dai, S. Aydin, M. Y. Yardımcı, R. Qiang, K. Lesage, and G. De Schutter, "Rheology, early-age hydration and microstructure of alkali-activated GGBFS-Fly ash-limestone mixtures," *Cem. Concr. Compos.*, vol. 124, no. May, p. 104244, 2021, doi: 10.1016/j.cemconcomp.2021.104244.

[7] X. Dai, S. Aydın, M. Y. Yardımcı, K. Lesage, and G. De Schutter, "Effects of activator properties and GGBFS/FA ratio on the structural build-up and rheology of AAC," *Cem. Concr. Res.*, vol. 138, no. October, p. 106253, 2020, doi: 10.1016/j.cemconres.2020.106253.

[8] X. Dai, S. Aydin, M. Y. Yardimci, and G. De Schutter, "Rheology and structural build-up of sodium silicate- and sodium hydroxide-activated GGBFS mixtures," *Cem. Concr. Compos.*, vol. 131, Aug. 2022, doi: 10.1016/j.cemconcomp.2022.104570.

[9] N. Roussel, G. Ovarlez, S. Garraul, C. Brumaud, "The origins of thixotropy of fresh cement pastes," *Cem. Concr. Res.*, no. 42, pp. 148–157, 2012, doi: 10.1016/j.cemconres.2011.09.004.

[10] M. F. Alnahhal, T. Kim, and A. Hajimohammadi, “Distinctive rheological and temporal viscoelastic behaviour of alkali-activated fly ash / slag pastes : A comparative study with cement paste,” *Cem. Concr. Res.*, vol. 144, no. March, p. 106441, 2021, doi: 10.1016/j.cemconres.2021.106441.

[11] A. Kashani, J. L. Provis, G. G. Qiao, and J. S. J. Van Deventer, “The interrelationship between surface chemistry and rheology in alkali activated slag paste,” *Constr. Build. Mater.*, vol. 65, pp. 583–591, 2014, doi: 10.1016/j.conbuildmat.2014.04.127.

[12] M. Palacios *et al.*, “Early reactivity of sodium silicate-activated slag pastes and its impact on rheological properties,” *Cem. Concr. Res.*, vol. 140, no. July 2020, p. 106302, 2021, doi: 10.1016/j.cemconres.2020.106302.

[13] N. Li, C. Shi, and Z. Zhang, “Understanding the roles of activators towards setting and hardening control of alkali-activated slag cement,” *Compos. Part B Eng.*, vol. 171, no. January, pp. 34–45, 2019, doi: 10.1016/j.compositesb.2019.04.024.

[14] W. Chen, B. Li, J. Wang, and N. Thom, “Effects of alkali dosage and silicate modulus on autogenous shrinkage of alkali-activated slag cement paste,” *Cem. Concr. Res.*, vol. 141, no. February 2020, 2021, doi: 10.1016/j.cemconres.2020.106322.

[15] F. Puertas, A. Fernández-Jiménez, and M. T. Blanco-Varela, “Pore solution in alkali-activated slag cement pastes. Relation to the composition and structure of calcium silicate hydrate,” *Cem. Concr. Res.*, vol. 34, no. 1, pp. 139–148, 2004, doi: 10.1016/S0008-8846(03)00254-0.

[16] I. Ismail, S. A. Bernal, J. L. Provis, R. San Nicolas, S. Hamdan, and J. S. J. Van Deventer, “Modification of phase evolution in alkali-activated blast furnace slag by the incorporation of fly ash,” *Cem. Concr. Compos.*, vol. 45, pp. 125–135, 2014, doi: 10.1016/j.cemconcomp.2013.09.006.

[17] J. Aupoil, J. B. Champenois, J. B. d’Espinose de Lacaillerie, and A. Poulesquen, “Interplay between silicate and hydroxide ions during geopolymerization,” *Cem. Concr. Res.*, vol. 115, no. May 2018, pp. 426–432, 2019, doi: 10.1016/j.cemconres.2018.09.012.

[18] M. Nehdi and M. A. Rahman, “Estimating rheological properties of cement pastes using various rheological models for different test geometry, gap and surface friction,” *Cem. Concr. Res.*, vol. 34, no. 11, pp. 1993–2007, 2004, doi: 10.1016/j.cemconres.2004.02.020.

[19] X. Dai, S. Aydin, M. Y. Yardımcı, and G. De Schutter, “Early Structural Build-up, Setting Behavior, Reaction Kinetics and Microstructure of Sodium Silicate-Activated Slag Mixtures with Different Retarder Chemicals,” *Cem. Concr. Res.*, vol. 159, p. 106872, 2022, doi:

624 10.1016/j.cemconres.2022.106872.
625 [20] X. Dai, S. Aydin, M. Y. Yardımcı, and G. De Schutter, “Rheology and structural build-up of sodium
626 silicate- and sodium hydroxide-activated GGBFS mixtures,” *Cem. Concr. Compos.*, vol. 131, no. May, p.
627 104570, 2022, doi: 10.1016/j.cemconcomp.2022.104570.
628 [21] *BS EN 196-3:2005 +A1:2008 Methods of testing cement — Part 3: Determination of setting times and*
629 *soundness*, vol. 3, no. August. 2003.
630 [22] M. Ezzat, X. Xu, K. El Cheikh, K. Lesage, R. Hoogenboom, and G. De Schutter, “Structure-property
631 relationships for polycarboxylate ether superplasticizers by means of RAFT polymerization,” *J. Colloid*
632 *Interface Sci.*, vol. 553, pp. 788–797, 2019, doi: 10.1016/j.jcis.2019.06.088.
633 [23] X. Chen, A. Meawad, and L. J. Struble, “Method to stop geopolymer reaction,” *J. Am. Ceram. Soc.*, vol.
634 97, no. 10, pp. 3270–3275, 2014, doi: 10.1111/jace.13071.
635 [24] R. J. Myers, S. A. Bernal, R. San Nicolas, and J. L. Provis, “Generalized structural description of
636 calcium-sodium aluminosilicate hydrate gels: The cross-linked substituted tobermorite model,”
637 *Langmuir*, vol. 29, no. 17, pp. 5294–5306, 2013, doi: 10.1021/la4000473.
638 [25] A. M. Mostafa and A. Yahia, “Physico-chemical kinetics of structural build-up of neat cement-based
639 suspensions,” *Cem. Concr. Res.*, vol. 97, pp. 11–27, 2017, doi: 10.1016/j.cemconres.2017.03.003.
640 [26] A. Favier, J. Hot, G. Habert, N. Roussel, and J. B. D’Espinose De Lacaillerie, “Flow properties of MK-
641 based geopolymer pastes. A comparative study with standard Portland cement pastes,” *Soft Matter*, vol.
642 10, no. 8, pp. 1134–1141, 2014, doi: 10.1039/c3sm51889b.
643 [27] Y. Zuo, M. Nedeljković, and G. Ye, “Pore solution composition of alkali-activated slag/fly ash pastes,”
644 *Cem. Concr. Res.*, vol. 115, no. October 2018, pp. 230–250, 2019, doi:
645 10.1016/j.cemconres.2018.10.010.
646 [28] P. Perez-Cortes and J. I. Escalante-Garcia, “Gel composition and molecular structure of alkali-activated
647 metakaolin-limestone cements,” *Cem. Concr. Res.*, vol. 137, no. August, p. 106211, 2020, doi:
648 10.1016/j.cemconres.2020.106211.
649 [29] B. S. Gebregziabiher, R. Thomas, and S. Peethamparan, “Very early-age reaction kinetics and
650 microstructural development in alkali-activated slag,” *Cem. Concr. Compos.*, vol. 55, pp. 91–102, 2015,
651 doi: 10.1016/j.cemconcomp.2014.09.001.
652 [30] X. Gao, Q. L. Yu, and H. J. H. Brouwers, “Properties of alkali activated slag-fly ash blends with
653 limestone addition,” *Cem. Concr. Compos.*, vol. 59, pp. 119–128, 2015, doi:

10.1016/j.cemconcomp.2015.01.007.

[31] X. Dai, S. Aydin, M. Y. Yardımcı, K. Lesage, and G. De Schutter, “Influence of water to binder ratio on the rheology and structural Build-up of Alkali-Activated Slag / Fly ash mixtures,” *Constr. Build. Mater.*, vol. 264, p. 120253, 2020, doi: 10.1016/j.conbuildmat.2020.120253.

[32] X. Dai, S. Aydın, M. Y. Yardımcı, K. Lesage, and G. De Schutter, “Rheology and microstructure of alkali-activated slag cements produced with silica fume activator,” *Cem. Concr. Compos.*, vol. 125, no. September 2021, p. 104303, 2022, doi: 10.1016/j.cemconcomp.2021.104303.

[33] X. Gao, Q. L. Yu, and H. J. H. Brouwers, “Reaction kinetics, gel character and strength of ambient temperature cured alkali activated slag-fly ash blends,” *Constr. Build. Mater.*, vol. 80, pp. 105–115, 2015, doi: 10.1016/j.conbuildmat.2015.01.065.

[34] S. A. Bernal, “Effect of the activator dose on the compressive strength and accelerated carbonation resistance of alkali silicate-activated slag/metakaolin blended materials,” *Constr. Build. Mater.*, vol. 98, pp. 217–226, 2015, doi: 10.1016/j.conbuildmat.2015.08.013.

[35] C. Shi and R. L. Day, “A calorimetric study of early hydration of alkali-slag cements,” *Cem. Concr. Res.*, vol. 25, no. 6, pp. 1333–1346, 1995.

[36] A. R. Brough and A. Atkinson, “Sodium silicate-based, alkali-activated slag mortars - Part I. Strength, hydration and microstructure,” *Cem. Concr. Res.*, vol. 32, no. 6, pp. 865–879, 2002, doi: 10.1016/S0008-8846(02)00717-2.

[37] S. Song and H. M. Jennings, “Pore solution chemistry of alkali-activated ground granulated blast-furnace slag,” *Cem. Concr. Res.*, vol. 29, no. 2, pp. 159–170, 1999, doi: 10.1016/S0008-8846(98)00212-9.

[38] R. Cao, S. Zhang, N. Banthia, Y. Zhang, and Z. Zhang, “Interpreting the early-age reaction process of alkali-activated slag by using combined embedded ultrasonic measurement , thermal analysis , XRD , FTIR and SEM,” *Compos. Part B*, vol. 186, no. November 2019, p. 107840, 2020, doi: 10.1016/j.compositesb.2020.107840.

[39] F. Puertas, M. Palacios, H. Manzano, J. S. Dolado, A. Rico, and J. Rodríguez, “A model for the C-A-S-H gel formed in alkali-activated slag cements,” *J. Eur. Ceram. Soc.*, vol. 31, no. 12, pp. 2043–2056, 2011, doi: 10.1016/j.jeurceramsoc.2011.04.036.

[40] B. Walkley, X. Ke, J. L. Provis, and S. A. Bernal, “Activator Anion Influences the Nanostructure of Alkali-Activated Slag Cements,” *J. Phys. Chem. C*, 2021, doi: 10.1021/acs.jpcc.1c07328.

[41] R. J. Myers, S. A. Bernal, J. D. Gehman, J. S. J. Van Deventer, and J. L. Provis, “The role of al in cross-

linking of alkali-Activated slag cements," *J. Am. Ceram. Soc.*, vol. 98, no. 3, pp. 996–1004, 2015, doi: 10.1111/jace.13360.

[42] P. S. Singh, T. I. M. Bastow, M. Trigg, and C. S. Mdc, "Structural studies of geopolymers by 29 Si and 27 Al MAS-NMR," vol. 0, pp. 3951–3961, 2005.

[43] X. Gao, Q. L. Yu, and H. J. H. Brouwers, "Apply 29 Si , 27 Al MAS NMR and selective dissolution in identifying the reaction degree of alkali activated slag- fly ash composites," *Ceram. Int.*, vol. 43, no. May, pp. 12408–12419, 2017, doi: 10.1016/j.ceramint.2017.06.108.

[44] E. L. Hôpital, B. Lothenbach, G. Le Saout, D. Kulik, and K. Scrivener, "Incorporation of aluminium in calcium-silicate-hydrates," *Cem. Concr. Res.*, vol. 75, pp. 91–103, 2015, doi: 10.1016/j.cemconres.2015.04.007.

[45] G. Fang and M. Zhang, "Multiscale micromechanical analysis of alkali-activated fly ash-slag paste," *Cem. Concr. Res.*, vol. 135, no. May, p. 106141, 2020, doi: 10.1016/j.cemconres.2020.106141.

[46] B. Walkley *et al.*, "Phase evolution of C-(N)-A-S-H/N-A-S-H gel blends investigated via alkali-activation of synthetic calcium aluminosilicate precursors," *Cem. Concr. Res.*, vol. 89, pp. 120–135, 2016, doi: 10.1016/j.cemconres.2016.08.010.

[47] G. Fang and M. Zhang, "Multiscale micromechanical analysis of alkali-activated fly ash-slag paste," *Cem. Concr. Res.*, vol. 135, no. June, p. 106141, 2020, doi: 10.1016/j.cemconres.2020.106141.

[48] X. Chen, A. Sutrisno, and L. J. Struble, "Effects of calcium on setting mechanism of metakaolin-based geopolymer," *J. Am. Ceram. Soc.*, vol. 101, no. 2, pp. 957–968, 2018, doi: 10.1111/jace.15249.

[49] X. Chen, A. Sutrisno, L. Zhu, and L. J. Struble, "Setting and nanostructural evolution of metakaolin geopolymer," *J. Am. Ceram. Soc.*, vol. 100, no. 5, pp. 2285–2295, 2017, doi: 10.1111/jace.14641.

[50] B. Walkley, R. San, M. Sani, J. D. Gehman, J. S. J. Van Deventer, and J. L. Provis, "Synthesis of stoichiometrically controlled reactive aluminosilicate and calcium-aluminosilicate powders," *Powder Technol.*, vol. 297, pp. 17–33, 2016, doi: 10.1016/j.powtec.2016.04.006.

[51] I. Garcia-Lodeiro, A. Palomo, A. Fernández-Jiménez, and D. E. MacPhee, "Compatibility studies between N-A-S-H and C-A-S-H gels. Study in the ternary diagram Na2O-CaO-Al2O3-SiO 2-H2O," *Cem. Concr. Res.*, vol. 41, no. 9, pp. 923–931, 2011, doi: 10.1016/j.cemconres.2011.05.006.

[52] A. Palomo, D. E. Macphee, and A. Ferna, "Effect of Calcium Additions on N–A–S–H Cementitious Gels," vol. 1940, pp. 1934–1940, 2010, doi: 10.1111/j.1551-2916.2010.03668.x.

[53] I. G. Richardson, A. R. Brough, G. W. Groves, and C. M. Dobson, "The characterization of hardened

alkali-activated blast-furnace slag pastes and the nature of the calcium silicate hydrate (C-S-H) phase," *Cem. Concr. Res.*, vol. 24, no. 5, pp. 813–829, 1994, doi: 10.1016/0008-8846(94)90002-7.

[54] I. G. Richardson and G. W. Groves, "The incorporation of minor and trace elements into calcium silicate hydrate (C-S-H) gel in hardened cement pastes," *Cem. Concr. Res.*, vol. 23, pp. 131–138, 1993.

[55] W. Mozgawa and J. Deja, "Spectroscopic studies of alkaline activated slag geopolymers," *J. Mol. Struct.*, vol. 924–926, no. C, pp. 434–441, 2009, doi: 10.1016/j.molstruc.2008.12.026.

[56] A. Fernandez-Jimenez and F. Puertas, "Structure of Calcium Silicate Hydrates Formed in Alkaline-Activated Slag : Influence of the Type of Alkaline Activator," *J. Am. Ceram. Soc.*, vol. 94, pp. 1389–1394, 2003.

[57] N. Li, N. Farzadnia, and C. Shi, "Microstructural changes in alkali-activated slag mortars induced by accelerated carbonation," *Cem. Concr. Res.*, vol. 100, no. July, pp. 214–226, 2017, doi: 10.1016/j.cemconres.2017.07.008.

[58] I. García Lodeiro, D. E. Macphee, A. Palomo, and A. Fernández-Jiménez, "Effect of alkalis on fresh C-S-H gels. FTIR analysis," *Cem. Concr. Res.*, vol. 39, no. 3, pp. 147–153, 2009, doi: 10.1016/j.cemconres.2009.01.003.

[59] S. Puligilla and P. Mondal, "Co-existence of aluminosilicate and calcium silicate gel characterized through selective dissolution and FTIR spectral subtraction," *Cem. Concr. Res.*, vol. 70, pp. 39–49, 2015, doi: 10.1016/j.cemconres.2015.01.006.

[60] N. K. Lee and H. K. Lee, "Reactivity and reaction products of alkali-activated, fly ash/slag paste," *Constr. Build. Mater.*, vol. 81, pp. 303–312, 2015, doi: 10.1016/j.conbuildmat.2015.02.022.

[61] B. Walkley, R. San Nicolas, and S. Bernal, "Effect of MgO incorporation on the structure of synthetic alkali-activated calcium aluminosilicate binders," *Conf. 27th Bienn. Natl. Conf. Concr. Inst. Aust.*, no. August 2015, 2015, [Online]. Available: https://www.researchgate.net/publication/303968983_Effect_of_MgO_incorporation_on_the_structure_of_synthetic_alkali-activated_calcium_aluminosilicate_binders.